

## Aberystwyth University

### *A deep learning-integrated micro-CT image analysis pipeline for quantifying rice lodging resistance-related traits*

Wu, Di; Wu, Dan; Feng, Hui; Duan, Lingfeng; Dai, Guoxing; Liu, Xiao; Wang, Kang; Yang, Peng; Chen, Guoxing; Gay, Alan P.; Doonan, John H.; Niu, Zhiyou; Xiong, Lizhong; Yang, Wanneng

*Published in:*  
Plant Communications

*DOI:*  
[10.1016/j.xplc.2021.100165](https://doi.org/10.1016/j.xplc.2021.100165)

*Publication date:*  
2021

*Citation for published version (APA):*

Wu, D., Wu, D., Feng, H., Duan, L., Dai, G., Liu, X., Wang, K., Yang, P., Chen, G., Gay, A. P., Doonan, J. H., Niu, Z., Xiong, L., & Yang, W. (2021). A deep learning-integrated micro-CT image analysis pipeline for quantifying rice lodging resistance-related traits. *Plant Communications*, [100165].  
<https://doi.org/10.1016/j.xplc.2021.100165>

#### **Document License** CC BY-NC-ND

#### **General rights**

Copyright and moral rights for the publications made accessible in the Aberystwyth Research Portal (the Institutional Repository) are retained by the authors and/or other copyright owners and it is a condition of accessing publications that users recognise and abide by the legal requirements associated with these rights.

- Users may download and print one copy of any publication from the Aberystwyth Research Portal for the purpose of private study or research.
- You may not further distribute the material or use it for any profit-making activity or commercial gain
- You may freely distribute the URL identifying the publication in the Aberystwyth Research Portal

#### **Take down policy**

If you believe that this document breaches copyright please contact us providing details, and we will remove access to the work immediately and investigate your claim.

tel: +44 1970 62 2400  
email: [is@aber.ac.uk](mailto:is@aber.ac.uk)

# A deep learning-integrated micro-CT image analysis pipeline for quantifying rice lodging resistance-related traits

Di Wu<sup>1,2,4</sup>, Dan Wu<sup>1,4</sup>, Hui Feng<sup>1</sup>, Lingfeng Duan<sup>1</sup>, Guoxing Dai<sup>1</sup>, Xiao Liu<sup>1</sup>, Kang Wang<sup>1</sup>, Peng Yang<sup>1</sup>, Guoxing Chen<sup>1</sup>, Alan P. Gay<sup>3</sup>, John H. Doonan<sup>3</sup>, Zhiyou Niu<sup>1</sup>, Lizhong Xiong<sup>1</sup> and Wanneng Yang<sup>1,\*</sup>

<sup>1</sup>National Key Laboratory of Crop Genetic Improvement, National Center of Plant Gene Research, Hubei Key Laboratory of Agricultural Bioinformatics and College of Engineering, Huazhong Agricultural University, Wuhan 430070, PR China

<sup>2</sup>School of Information Engineering, Wuhan Technology and Business University, Wuhan 430065, PR China

<sup>3</sup>The National Plant Phenomics Centre, Institute of Biological, Environmental and Rural Sciences, Aberystwyth University, Aberystwyth, UK

<sup>4</sup>These authors contributed equally to this article.

\*Correspondence: Wanneng Yang ([ywn@mail.hzau.edu.cn](mailto:ywn@mail.hzau.edu.cn))

<https://doi.org/10.1016/j.xplc.2021.100165>

## ABSTRACT

Lodging is a common problem in rice, reducing its yield and mechanical harvesting efficiency. Rice architecture is a key aspect of its domestication and a major factor that limits its high productivity. The ideal rice culm structure, including major\_axis\_culm, minor\_axis\_culm, and wall\_thickness\_culm, is critical for improving lodging resistance. However, the traditional method of measuring rice culms is destructive, time consuming, and labor intensive. In this study, we used a high-throughput micro-CT-RGB imaging system and deep learning (SegNet) to develop a high-throughput micro-CT image analysis pipeline that can extract 24 rice culm morphological traits and lodging resistance-related traits. When manual and automatic measurements were compared at the mature stage, the mean absolute percentage errors for major\_axis\_culm, minor\_axis\_culm, and wall\_thickness\_culm in 104 *indica rice* accessions were 6.03%, 5.60%, and 9.85%, respectively, and the  $R^2$  values were 0.799, 0.818, and 0.623. We also built models of bending stress using culm traits at the mature and tillering stages, and the  $R^2$  values were 0.722 and 0.544, respectively. The modeling results indicated that this method can quantify lodging resistance nondestructively, even at an early growth stage. In addition, we also evaluated the relationships of bending stress to shoot dry weight, culm density, and drought-related traits and found that plants with greater resistance to bending stress had slightly higher biomass, culm density, and culm area but poorer drought resistance. In conclusion, we developed a deep learning-integrated micro-CT image analysis pipeline to accurately quantify the phenotypic traits of rice culms in ~4.6 min per plant; this pipeline will assist in future high-throughput screening of large rice populations for lodging resistance.

**Keywords:** rice culm, micro-CT, lodging resistance, SegNet, high-throughput, deep learning

Wu D., Wu D., Feng H., Duan L., Dai G., Liu X., Wang K., Yang P., Chen G., Gay A.P., Doonan J.H., Niu Z., Xiong L., and Yang W. (2021). A deep learning-integrated micro-CT image analysis pipeline for quantifying rice lodging resistance-related traits. *Plant Comm.* **2**, 100165.

## BACKGROUND

Rice is the main staple food for most of the world's population (Zhang, 2007). To keep pace with rapid population growth and mitigate the negative effects of global climate change on crop yield, it is important to increase yield potential and the reliability of production (Brown and Funk, 2008; Beddington, 2010). Lodging, in which crops fall over, occurs when the bending force exerted by strong wind on the plant exceeds the strength of the

stem or the anchorage in the soil. Lodging is a problem in cereals, reducing the harvestable yield and thus the reliability of production. In rice, lodging is known to reduce mechanical harvesting efficiency (Kashiwagi et al., 2004) and disrupt canopy architecture (Liu et al., 2018). The maintenance of an appropriate

Published by the Plant Communications Shanghai Editorial Office in association with Cell Press, an imprint of Elsevier Inc., on behalf of CSPB and CEMPS, CAS.

## Plant Communications

architecture is a major factor in maximizing productivity, and architecture has been improved during the domestication of rice (Wang et al., 2008; Li et al., 2003; Wang et al., 2005).

The ability of structural improvements to reduce stem lodging was demonstrated in the “Green Revolution,” in which major alleles in the gibberellin pathway were modified to produce dwarf stems, which in turn reduced lodging under conditions of high nitrogen and yield (Hedden, 2013). The possibility that further height reduction might decrease lodging risk has been considered, but it is also likely to reduce yield (Berry et al., 2007). It is therefore worth focusing on detailed structural characteristics that might be modified to increase stem strength. However, measurement of these traits is destructive, time consuming, and labor intensive (Houle et al., 2010; Furbank and Tester, 2011). For example, measurements of the major and minor diameters of the elliptical cross-section and the wall thickness of the stem must be obtained manually with Vernier calipers and may therefore be somewhat subjective as well as destructive. In addition, bending stress is typically measured with a prostrate tester, which measures a group of stems destructively (Kashiwagi et al., 2004; Duan et al., 2004). To address the challenge of screening high numbers of rice genotypes, a rapid, nondestructive phenotyping tool is needed for screening the structural characteristics of rice stems.

The monitoring of rice lodging has been improved by the use of imaging sensors mounted on unmanned aerial vehicles (Li et al., 2014; Chu et al., 2017). This process has advanced with the use of high-resolution digital and multispectral cameras to map areas of lodging in rice crops for disaster-relief purposes (Yang et al., 2017). In addition, visible and thermal infrared images have been used to establish lodging percentages that allow comparisons between two varieties of rice (Liu et al., 2018). However, although monitoring the amount of lodging is useful for revising crop forecasts, in the longer term it is important to breed crops that do not lodge in the first place. In addition, the effect of a given combination of lodging forces will increase as grain filling occurs because greater leverage is exerted on the stem as grain weight increases. Thus, increasing lodging resistance by improving the structural strength of plants is a focus of breeding programs and requires nondestructive and accurate phenotyping techniques.

X-ray CT has the potential to provide such measurements in a scalable fashion because it requires no direct contact, is relatively quick to implement, and is inherently nondestructive. X-ray CT has already been used to detect and quantify the inner structures of shoots, organs, and roots from the cellular to the whole-organ scale. For example, the structure of xylem vessels and the frequency of embolism can be rapidly assessed in maize leaves (Ryu et al., 2016). This technology has also provided detailed internal three-dimensional (3D) phenotypic information for flowers (Tracy et al., 2017), grains (Hughes et al., 2017), spikes (Strange et al., 2015), and stalks (Zhang et al., 2018) in a nondestructive manner. X-ray CT scanning has also been used in studies of root lodging aimed at determining the structure of roots in soil (Lontoc-Roy et al., 2006; Flavel et al., 2012), quantifying compaction (Tracy et al., 2012, 2015), and investigating the effect of the rhizosphere on soil hydraulic properties (Daly et al., 2015).

## Micro-CT for rice lodging phenotyping

How to process huge numbers of raw CT images and detect the target organ is the next challenge. In the past few years, deep learning with convolutional neural networks (CNNs) has been widely used in crop organ detection (Kamilaris and Francesc, 2018); examples include the detection and quantification of soybean seed numbers (Uzal et al., 2018) and the counting of fruit (Rahneemoonfar and Sheppard, 2017). Faster R-CNN (Ren et al., 2017) has also been used to detect maize tassels (Liu et al., 2020), tomato diseases (Wang and Qi, 2019), and maize stems (Jin et al., 2018). To the best of our knowledge, a combination of CT images and deep learning has not previously been used to quantify structures related to rice stem lodging.

In our previous work, we developed an efficient and effective micro-CT-RGB imaging system that included CT scanning and RGB imaging in one chamber and could be used to quantify tiller growth nondestructively in whole rice populations (Wu et al., 2019). Here, we describe the application of this system to extract lodging-related stem morphological traits, focusing on culm (Wang et al., 2005) lodging. In particular, we use deep learning to improve the speed and accuracy of the segmentation between stem components and background, a critical requirement for the routine use of the system. This technology is scalable and could be adopted to screen large diversity sets or mapping populations, thereby assisting in the breeding of rice and other crops.

## RESULTS

### Image analysis pipeline and trait extraction

A high-throughput micro-CT system was developed to extract rice tiller growth traits in our previous work (Wu et al., 2019). Here, 104 rice accessions were inspected at the mature stage (approximately 120 days after sowing) to acquire lodging-related traits. For each sample, we reconstructed 80 slices (80 transverse sections of equally spaced rice culms obtained 50–118 mm from the soil surface, 1803 × 1803 pixels per slice). After 80 reconstructed CT images of each sample were obtained, the CT image analysis pipeline for lodging-related traits consisted of six steps (Figure 1): (1) 200 rice stem cross-sections were randomly selected and used to train and test the Culms-SegNet model using SegNet architecture (Vijay et al., 2017); (2) each original image (1803 × 1803 pixels) was enlarged and divided into 24 patches (480 × 360 pixels) to meet the input format of SegNet; (3) after data augmentation, a total of 10 173 patches, 480 patches, and 480 patches were used as the training set, validation set, and test set, respectively (more details of the Culms-SegNet construction are provided in the Methods section); (4) a total of 104 rice samples and 8320 images were automatically segmented by a well-trained Culms-SegNet model (Supplemental Note 2); (5) noise points (such as leaf sheaths) surrounding the culms (i.e., rice plant stems) were removed; and (6) after 80 slices were segmented for each plant, segmented 3D images of the rice culms were obtained. Supplemental Figure 1 shows the comparison to the original CT image, the manual segmentation, and the SegNet segmentation.

Figure 1N shows the reconstructed 3D images of the rice culms obtained by micro-CT and used to extract 24 culm traits (Table 1). The specified plant area (red box) in Figure 2A is the region of interest detected by micro-CT, and the height ranges

## Micro-CT for rice lodging phenotyping

## Plant Communications

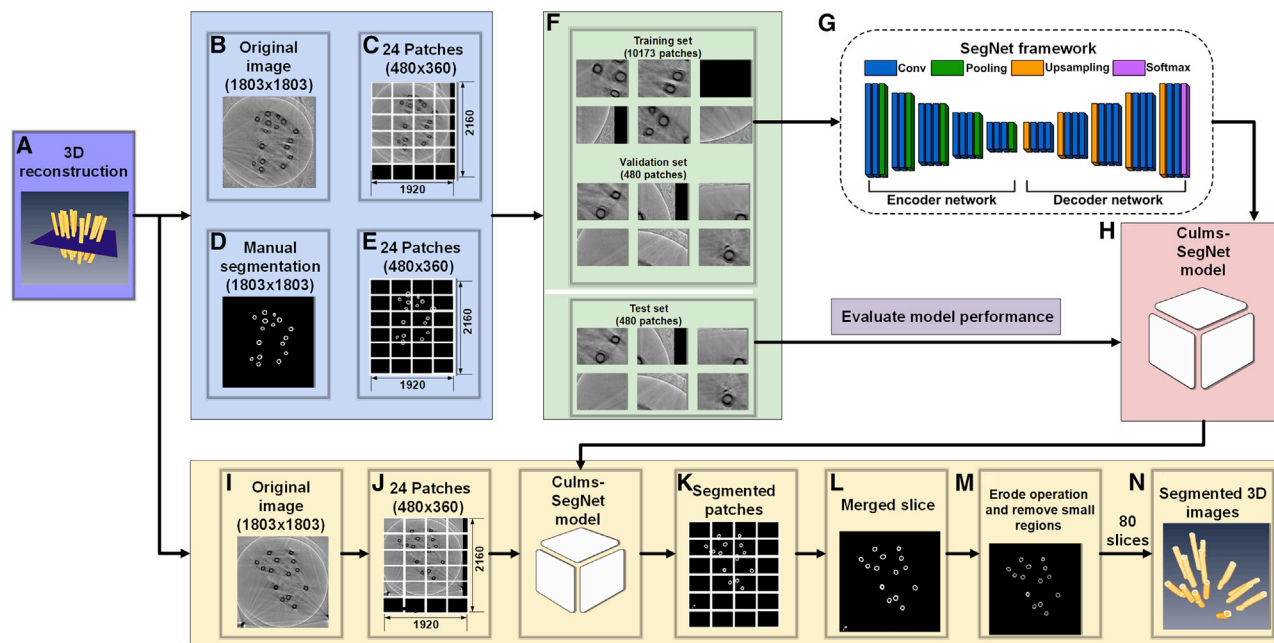


**Figure 1. The CT image analysis pipeline.**

(A) 3D reconstruction image; (B) 2D original image; (C and E) image extending, dividing, and input of the training set, validation set, and test set; (F and H) offline training with SegNet to obtain the trained Culms-SegNet model; (I) 2D original image; (J and K) image extending, dividing, and online segmentation with the Culms-SegNet model; (L and M) merging of segmented patches into a segmented slice, with the removal of small regions and erosion operation; and (N) 3D segmented image.

from 50 to 118 mm above the soil surface. As shown in Figure 2B and 2C, the main rice culm traits were calculated as follows: (1) *major\_axis\_culm* was the length of the minimum circumscribed rectangle of each culm; (2) *minor\_axis\_culm* was the width of the minimum circumscribed rectangle of each culm; and (3) culm diameter was calculated as:

$$\text{culm diameter} = (\text{major\_axis\_culm} + \text{minor\_axis\_culm}) / 2. \quad (\text{Equation 1})$$

The *major\_axis\_cavity* and *minor\_axis\_cavity* were the length and width of the minimum circumscribed rectangle of each culm cavity, and the cavity diameter was calculated as:

$$\text{cavity diameter} = (\text{major\_axis\_cavity} + \text{minor\_axis\_cavity}) / 2. \quad (\text{Equation 2})$$

Finally, *wall\_thickness\_culm* was calculated as:

$$\text{wall\_thickness\_culm} = (\text{culm diameter} - \text{cavity diameter}) / 2. \quad (\text{Equation 3})$$

All the culm traits are listed in Table 1, and the main source code is provided in Supplemental Note 2.

### Measuring the accuracy of *major\_axis\_culm*, *minor\_axis\_culm*, and *wall\_thickness\_culm*

To evaluate the measurement accuracy of *major\_axis\_culm*, *minor\_axis\_culm*, and *wall\_thickness\_culm*, 104 rice accessions were automatically measured by micro-CT and manually

measured. The scatterplots of the automatic measurements versus the manual measurements for *major\_axis\_culm*, *minor\_axis\_culm*, and *wall\_thickness\_culm* are provided in Figure 2D–2F. The squares of the correlation coefficients ( $R^2$ ), the mean absolute percentage error (MAPE), and the root-mean-square error (RMSE) were 0.623–0.818, 5.605%–9.846%, and 0.104–0.518 mm, respectively. The computational formulas of MAPE and RMSE are defined by Equations 4 and 5:

$$\text{MAPE} = \frac{1}{n} \sum_{i=1}^n \frac{|x_{ai} - x_{mi}|}{x_{mi}} \times 100\%; \quad (\text{Equation 4})$$

$$\text{RMSE} = \sqrt{\frac{1}{n} \sum_{i=1}^n (x_{ai} - x_{mi})^2}. \quad (\text{Equation 5})$$

In Equations 4 and 5,  $x_{mi}$  is the manually measured value,  $x_{ai}$  is the automatically measured value, and  $n$  is the number of rice accessions.

Frequency plots of the absolute percentage error for *major\_axis\_culm*, *minor\_axis\_culm*, and *wall\_thickness\_culm* are shown in Figure 2G–2I. As shown in the frequency plots, the absolute percentage error of 80% of the rice accessions was less than 10%, 10%, and 15% for *major\_axis\_culm*, *minor\_axis\_culm*, and *wall\_thickness\_culm*, respectively. The original data are provided in Supplemental Data 1.

### Modeling bending stress at the mature stage

To investigate bending stress (which reflects lodging resistance) (Kashiwagi et al., 2004) using nondestructively measured CT

Definition and calculation	Abbreviation
Maximum value of culm wall area (sum of culm wall pixels) for all culms	max_area_culm
Mean value of culm wall area (sum of culm wall pixels) for all culms	mean_area_culm
SD of culm wall area (sum of culm wall pixels) for all culms	SD_area_culm
Maximum value of culm wall area (sum of culm wall pixels)/perimeter (sum of pixels around the culm wall) ratio for all culms	max_APR_culm
Mean value of culm wall area (sum of culm wall pixels)/perimeter (sum of pixels around the culm wall) ratio for all culms	mean_APR_culm
SD value of culm wall area (sum of culm wall pixels)/perimeter (sum of pixels around the culm wall) ratio for all culms	SD_APR_culm
Convex hull area surrounding all culms (sum of convex hull pixels)	CHA_culm
Total culm wall area (sum of total culm wall pixels)/convex hull area surrounding all culms (sum of convex hull pixels) ratio	CHR_culm
Total culm wall area (sum of total culm wall pixels)/circumcircle area (sum of circumcircle pixels) ratio	CCR_culm
Total culm wall area (sum of total culm wall pixels) for all culms	total_area_culm
Tiller number for all culms (the number of connected regions)	TN
Mean value of culm diameter for the largest three culms	mean_diameter_culm
Maximum value of culm diameter for the largest three culms	max_diameter_culm
SD of culm diameter for the largest three culms	SD_diameter_culm
Mean value of max_area_culm for the largest three culms	max_area_culm
Mean value of minor_axis_culm for the largest three culms	minor_axis_culm
Mean value of wall_thickness_culm for the largest three culms	wall_thickness_culm
Mean value of culm angle for all culms	MEANTA
Maximum value of culm angle for all culms	MAXTA
SD value of culm angle for all culms	SDTA
Total volume for all culms (sum of total culm wall pixels at all heights)	total_volume_culm
Total surface area for all culms (sum of total pixels around the culm wall at all heights)	total_SA_culm
Mean of gray values of all culm pixels	culm_density_mean
Sum of gray values of all culm pixels	culm_density_total

**Table 1. Twenty-four 3D culm traits measured by the micro-CT system.**



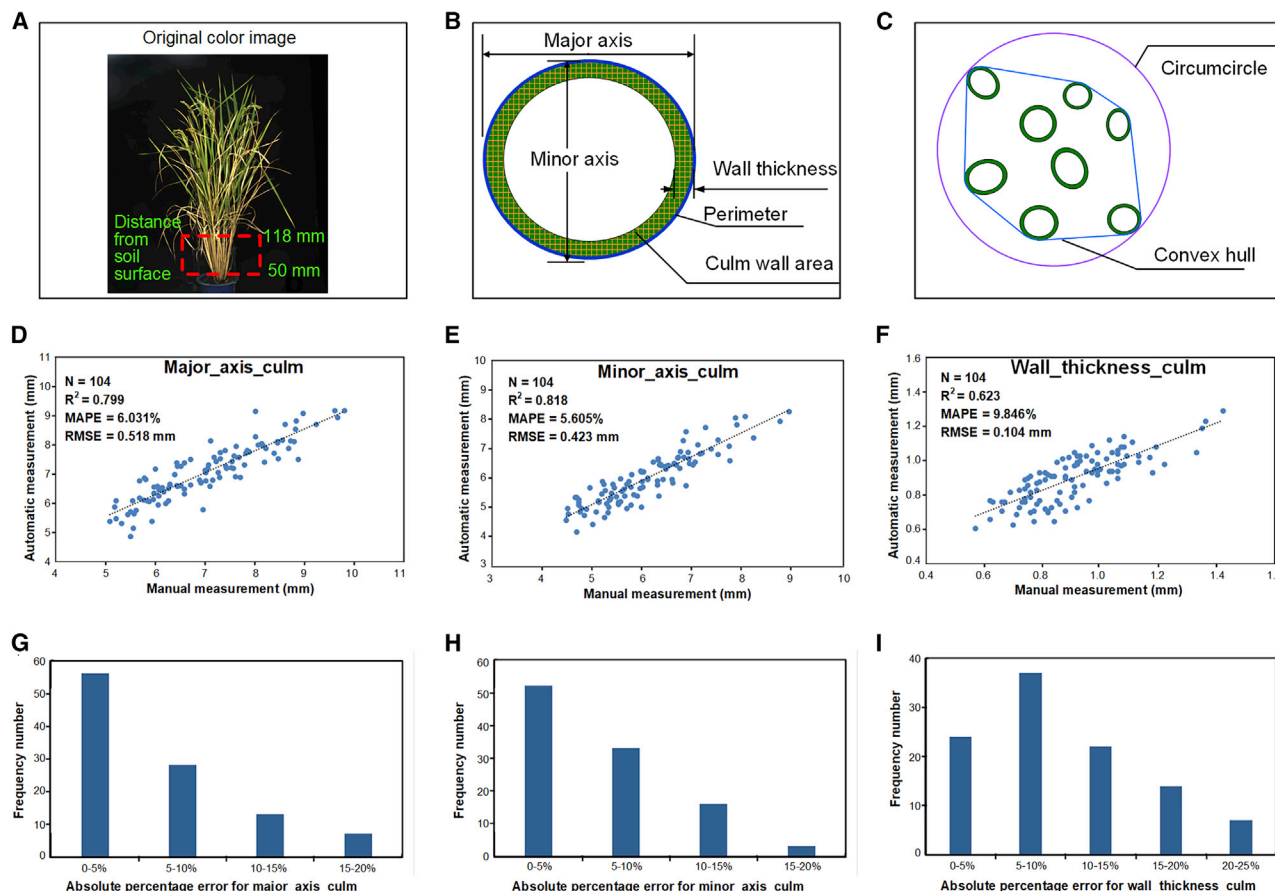


**Figure 2. Explanation of culm traits and performance evaluation of rice culm 3D trait extraction.**

(A) Original color image; (B and C) trait extraction and illustration. The red box is the region of interest detected by micro-CT, and the height ranges from 50 to 118 mm above the soil surface. Scatterplots of automatic versus manual measurements of mean values of (D) major\_axis\_culm, (E) minor\_axis\_culm, and (F) wall\_thickness\_culm made by the CT system. Frequency plots of rice culm mean values of (G) major\_axis\_culm, (H) minor\_axis\_culm, and (I) wall\_thickness\_culm obtained by the CT system.

traits, 104 rice accessions were tested at the mature stage, and all 24 3D CT traits were used for linear stepwise regression analysis (SPSS v.19, IBM, USA). After each sample was inspected by micro-CT, the bending stress was measured destructively using a prostrate tester (DIK-7401, Daiki Rika Kogyo, Japan). Up to 72.2% of the phenotypic variation in bending stress at the mature stage could be explained using two traits: mean\_area\_culm and MAXTA (maximum value of culm angle for all culms) (Figure 3A). The 104 accessions were divided into two groups: 50 accessions with higher resistance to bending stress (1113–3534 g) and 54 accessions with lower resistance to bending stress (195–1067 g). Statistical analyses showed a significant difference in mean\_area\_culm ( $t$ -test,  $P < 0.01$ ) and MAXTA ( $t$ -test,  $P < 0.05$ ) between these two groups. As shown in Figure 3B, the plants with higher resistance to bending stress had a higher mean\_area\_culm (reflecting thicker stems) and a lower MAXTA (reflecting more erect stems) than those with lower resistance.

We used three methods to evaluate the classification accuracy of bending stress: stepwise discriminant analysis (SDA) (Mallios, 2001; Shi et al., 2006), support vector machine (SVM) (Fung and Mangasarian, 2005; Iosifidis and Gabbouj, 2016), and random forest (RF) (Graniotto et al., 2006; Pardo and

Sberveglieri, 2008). Based on the modeling results in Figure 3A, two traits (mean\_area\_culm and MAXTA) were selected. When these traits were used, as shown in Figure 3C, the final leave-one-out cross-validation classification accuracies at the mature stage were 87.5%, 83.7%, and 80.8% for SDA, SVM, and RF, respectively. Among the three methods, SDA had better classification accuracy for rice culm bending stress than SVM and RF.

### Prediction of bending stress at the tillering stage

It would be helpful for rice breeding if we could predict bending stress at early developmental stages. In our previous work, 234 rice accessions were tested at the tillering stage using micro-CT and an RGB camera (Wu et al., 2019). Seventeen tiller traits (extracted by micro-CT) and 58 plant architecture traits (extracted from RGB images) of the same 104 *indica* rice accessions were selected and analyzed. We used 58 rice phenotypic traits at the tillering stage to evaluate the bending stress model by linear stepwise regression analysis (SPSS v.19, IBM). Scatterplots of the automatic measurements versus the manual measurements of RGB traits are shown in Supplemental Figure 2A. Up to 48.5% of the phenotypic variation in bending stress could be explained by combining five traits. Scatterplots of the automatic measurements versus the manual measurements for

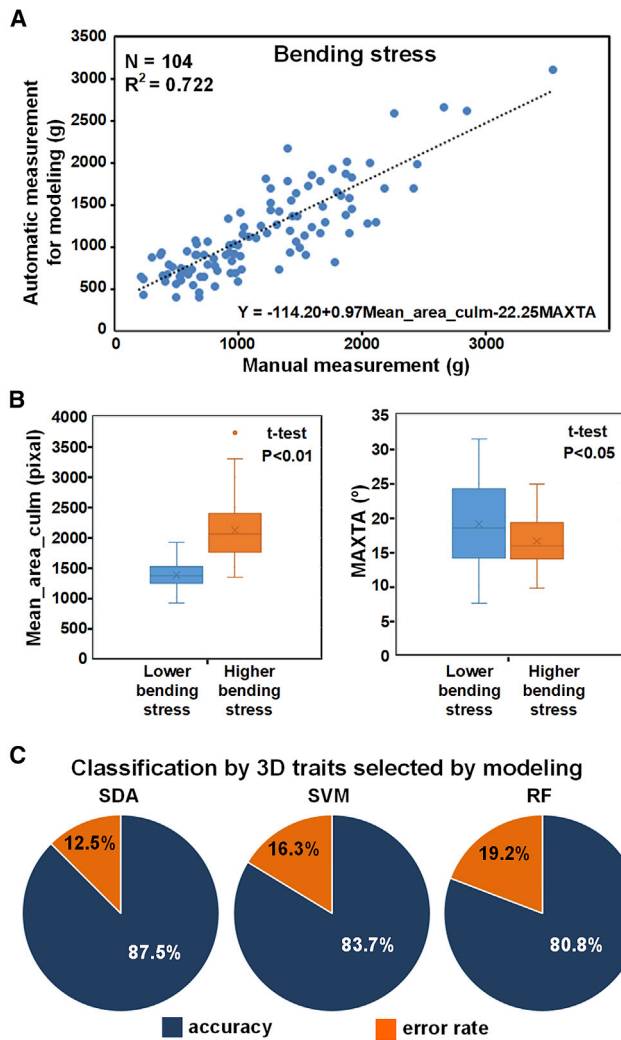


**Figure 3. Modeling of bending stress with two culm traits at the mature stage.**

(A) The modeling result of bending stress at the mature stage, (B) effects of higher and lower resistance to bending stress on mean\_area\_culm and MAXTA, and (C) classification results of stepwise discriminant analysis (SDA), support vector machine (SVM), and random forest (RF) with two culm traits.

CT and CT + RGB traits are shown in Supplemental Figure 2B and 2C. Up to 40.1% and 54.4% of the phenotypic variation in bending stress could be explained by combining three CT traits (MAXCD, tiller number, and MAXTA) and five CT + RGB traits, respectively. The detailed procedure for stepwise regression analysis is shown in Supplemental Table 1.

We also used SDA, SVM, and RF to classify bending stress. As shown in Supplemental Figure 3, when five RGB traits selected by modeling were used, the final leave-one-out cross-validation classification accuracies at the tillering stage were 75.0%, 68.3%, and 73.1% for SDA, SVM, and RF, respectively. When three CT traits and five CT + RGB traits selected by modeling were used, the final leave-one-out cross-validation classification accuracies at the tillering stage were 70.2%–74.0% and 72.1%–76.0% for CT and CT + RGB, respectively. In general, the classi-

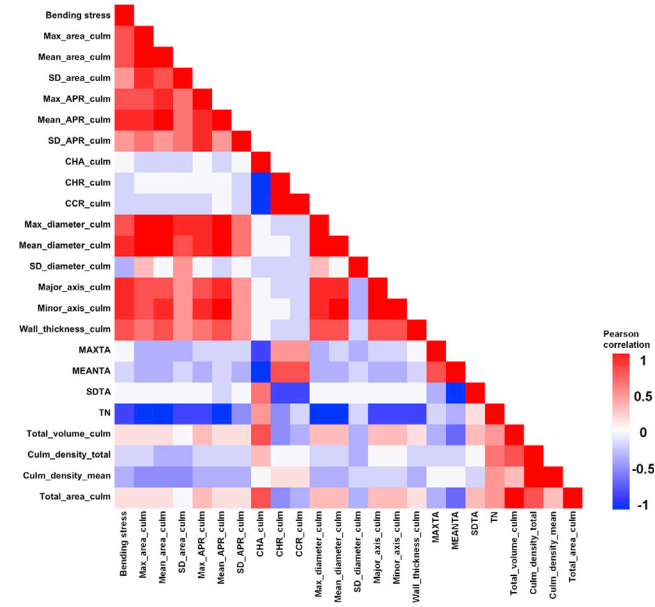


**Figure 4. Heatmap of correlations between bending stress and 24 3D rice culm traits extracted by micro-CT.**

fication accuracy for bending stress was lower at the tillering stage than at the mature stage. However, when CT traits and RGB traits were combined, we could infer bending stress at the tillering stage with a relatively high  $R^2$  (up to 0.544).

### Correlations among rice culm traits measured by the micro-CT system

The Pearson correlations ( $r$ ) between bending stress and 24 3D rice culm traits measured by micro-CT are illustrated in Figure 4. Bending stress was highly positively correlated with eight rice culm morphological traits (major\_axis\_culm, minor\_axis\_culm, wall\_thickness\_culm, mean\_diameter\_culm, max\_diameter\_culm, mean\_area\_culm, max\_area\_culm, and mean\_APR\_culm), all of which reflected culm thickness. Pearson correlation coefficients between bending stress and the eight rice culm traits ranged from 0.748 to 0.831. Tiller number was negatively correlated with the eight rice culm morphological traits and with bending stress; the corresponding values of  $r$  ranged from  $-0.650$  to  $-0.454$ , indicating that, among these 104 *indica* rice accessions, plants with more tillers often had smaller and thinner culms. More interestingly, we found that CHR\_culm and CCR\_culm (which reflect culm compactness) were negatively correlated with MEANTA and MAXTA (which reflect the culm angle), with  $r$  values from  $-0.748$  to  $-0.428$ . Therefore, plants with a more compact architecture (larger CHR\_culm and CCR\_culm values) also had more erect culms (smaller MEANTA and MAXTA values). Image acquisition was developed using Heml 1.0 (The CUCKOO Workgroup, Huazhong University of Science and Technology, PR China).

### Comparison of micro-CT and RGB-manual measurements of rice culm diameter

A comparison of the micro-CT and RGB-manual methods for measuring rice culm diameter is shown in Figure 5. The  $R^2$

## Micro-CT for rice lodging phenotyping

## Plant Communications

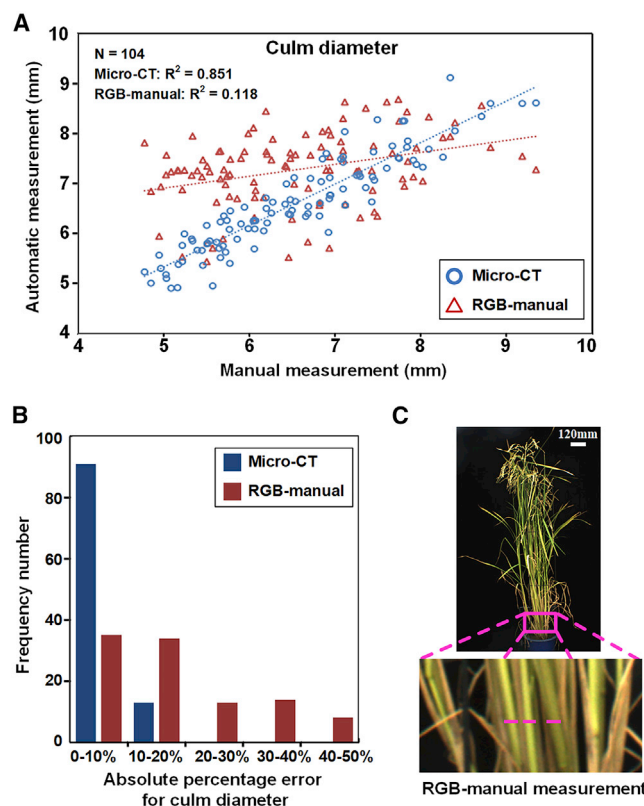


**Figure 5. Comparison of tiller diameter measurements by the micro-CT and RGB-manual methods.**

(A) Scatterplots of automatic versus manual measurements of rice culm diameter by the micro-CT and RGB-manual methods, (B) frequency plots of rice culm diameter measured by the micro-CT and RGB-manual methods, and (C) illustration of RGB-manual measurements of culm diameter.

values for micro-CT and RGB-manual measurements of rice culm diameter were 0.851 and 0.118, respectively, and the MAPE values were 5.230% and 17.720% (Figure 5A). Frequency plots of rice culm diameter are shown in Figure 5B. The absolute percentage error for rice culm diameter measured by micro-CT (blue column graph) was less than 20%, whereas the absolute percentage error for rice culm diameter measured by the RGB-manual method (red column graph) was less than 50%. Clearly, the accuracy of rice diameter measurement was much higher with micro-CT, which provides more transverse section information for rice culms. All rice plants were cultivated in plastic pots with three iron poles to avoid rice culm lodging (Figure 5C). The CT scan images appear very noisy and full of artifacts because of the three poles; these noises are difficult to remove but can easily be dealt with using the deep learning method.

## DISCUSSION

### Relationships between bending stress and shoot dry weight, culm density, and drought-related traits

After inspection by micro-CT, all 104 rice plants were cut and oven-dried to measure their shoot dry weights. Figure 6A shows that there was a significant difference in shoot dry weight between the higher and lower bending stress resistance groups ( $t$ -test,

$P < 0.01$ ). Plants with higher resistance to bending stress (red) had higher shoot dry weights, indicating that thicker culms contributed relatively more biomass. In addition to culm size, thickness, and angle, culm density can also be measured by micro-CT. *culm\_density\_mean* is the mean of the gray values (culm electron density) of all culm pixels in the reconstructed CT image, and *culm\_density\_total* is the sum of the gray values of all culm pixels in the image. Figure 6B and 6C show that there was a significant difference in *culm\_density\_mean* ( $t$ -test,  $P < 0.01$ ) and *culm\_density\_total* ( $t$ -test,  $P < 0.01$ ) between the higher and lower bending stress resistance groups. Plants with higher resistance to bending stress (red) had a slightly higher *culm\_density\_mean* (higher culm density) and *culm\_density\_total* (higher culm density and culm area) than those with lower resistance to bending stress. CT images of three different density materials are shown in Supplemental Figure 4.

In our previous work on 533 rice accessions, we obtained three drought-related traits: the green projected area ratio (GP<sub>AR</sub><sub>R</sub>, which reflects the stay-green phenotype and drought tolerance), total projected area/bounding rectangle area ratio (TBR<sub>R</sub>, which reflects leaf rolling and drought avoidance), and leaf water content (LWC) (Guo et al., 2018). Here, the three drought-related traits of the same 104 *indica* rice accessions were reanalyzed and compared in terms of bending stress. Figure 6D–6F shows that there were significant differences in GP<sub>AR</sub><sub>R</sub> ( $t$ -test,  $P < 0.01$ ), TBR<sub>R</sub> ( $t$ -test,  $P < 0.05$ ), and LWC ( $t$ -test,  $P < 0.01$ ) between the higher and lower bending stress resistance groups. Plants with higher resistance to bending stress (red) had a slightly lower GP<sub>AR</sub><sub>R</sub> (poorer drought tolerance), higher TBR<sub>R</sub> (poorer drought avoidance), and lower LWC (poorer drought tolerance). We could also infer that, among the tested accessions, plants with relatively more biomass had better bending stress resistance but poorer drought resistance because their relatively thicker culms lost water more easily under drought stress.

### Evaluation of the calculated culm area at different heights

For manual measurements of rice culm traits such as *major\_axis\_culm*, *minor\_axis\_culm*, and *wall\_thickness\_culm*, 40 individual rice culms were cut in the middle of the third internode (approximately 50 mm from the soil surface), and rice culm traits were measured destructively (Duan et al., 2004). The manual measurements of rice culms were labor intensive, time consuming, and poorly repeatable. Using micro-CT, we measured the traits of all rice culms at the 3D level, including the culm area. Figure 7 shows the distribution of culm wall area at different heights for different tillers (Beizinu cultivar, 50–118 mm distance from the soil surface). As illustrated in Figure 7A, the culm areas could be nondestructively obtained at heights ranging from 50 to 118 mm, thereby more accurately quantifying the variation in culm size between each pair of internodes. Interestingly, several clear peaks (red arrows) can be seen in Figure 7B and 7C, which indicate the node position of each rice culm within the larger area. In the future, if the micro-CT field of view were extended vertically and whole rice culms were screened and reconstructed, the node position, node length, and other node traits for all culms could also be obtained nondestructively. Also, the 3D bending stress



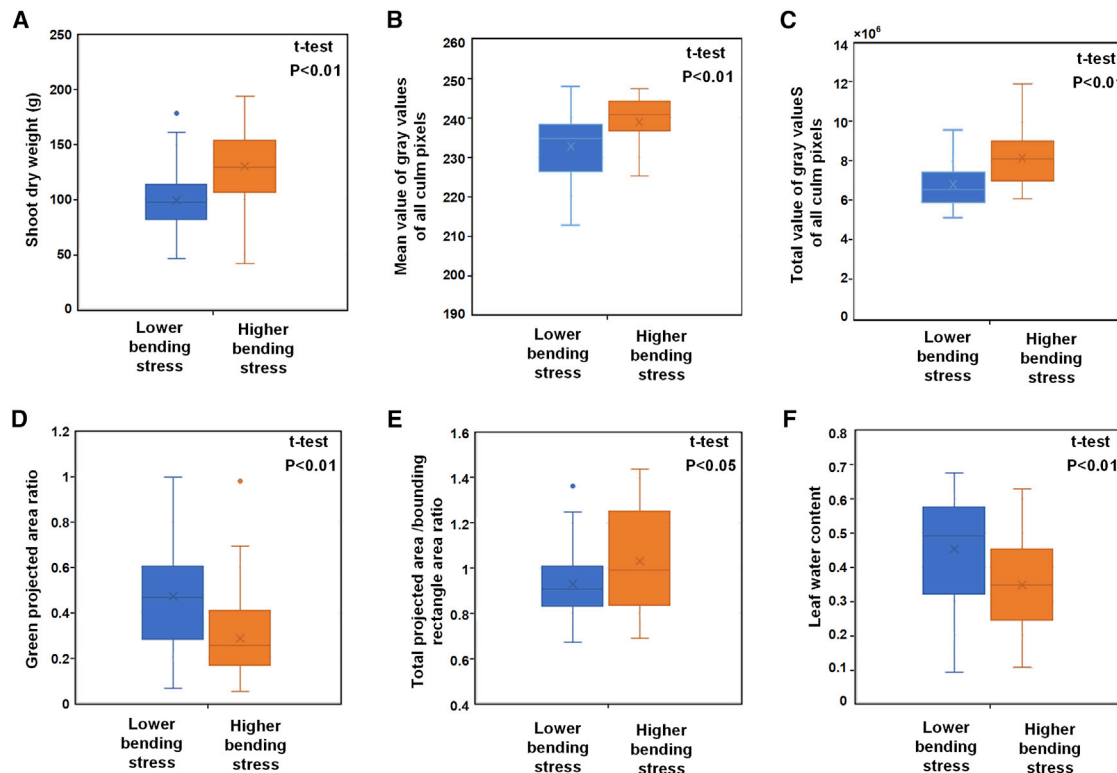


**Figure 6. The relationships between bending stress and shoot dry weight, culm density, and drought-related traits.**

Effects of higher and lower resistance to bending stress on the (A) shoot dry weight, (B) mean of gray values of all culm pixels, (C) sum of gray values of all culm pixels, (D) green projected area ratio, (E) total projected area/bounding rectangle area ratio, and (F) leaf water content.

distribution could be visualized through 3D heatmaps of rice culm wall area at different heights of rice culms. Figure 7D and 7G show a rice accession with lower bending stress resistance (Xiangzaoxian7hao) and an accession with higher bending stress resistance (BERLIN) at the mature stage. Based on the calculated rice culm wall area of 80 slices, a 3D heatmap of the rice culm wall area was obtained (Figure 7E and 7H). In the 3D heatmap, the red color indicates higher rice culm wall area (higher resistance to bending stress), and the blue color indicates lower rice culm wall area (lower resistance to bending stress). It is clear that BERLIN had a higher resistance to bending stress. In addition, the bending stress of a single culm is also shown in Figure 7F and 7I, which clearly show the strong and weak parts of a single culm.

Compared with the traditional method of measuring rice culm bending stress at a fixed height (50 mm from the soil surface), our method can measure all culm wall areas within a certain range and can evaluate the bending stress of the rice culm from a 3D perspective. By measuring differences in culm wall area at different heights, the location of the rice culm with the lowest bending stress resistance can be predicted accurately. Therefore, our method is potentially more accurate than the traditional manual method of assessing bending stress resistance of the rice culm.

### Processing efficiency of the image analysis pipeline

In this work, the time cost of image analysis for each plant could be divided into four parts: image reconstruction, image

segmentation with Culms-SegNet, trait extraction, and 3D data visualization. These steps required approximately 2.2, 0.1, 0.1, and 0.1 min, respectively (Microsoft Windows 10 PC with a 12-core Intel i7-6850K CPU, 3.6 GHz per CPU core, 32 GB of memory, and an Nvidia Titan Xp video card). There is a trade-off between reconstruction resolution and time/storage consumption. The time cost and storage cost increase if more slices are reconstructed; for example, the reconstruction and analysis of 1536 slices require 36 min on the hardware described above and 3.9 GB of storage (2.6 MB per slice). In this paper, our purpose was to evaluate lodging-related traits with a high-throughput method and a low number of reconstructed slices. For other purposes, such as measuring the vascular bundles of maize stalks (Du et al., 2016), the slice number and spatial resolution of micro-CT should be set at a higher level.

### CT image-based trait measurement for rice breeding and other applications

The micro-CT system can nondestructively measure culm area traits at different heights and predict the possible lodging point at an early stage, comprehensively characterizing the lodging resistance of the rice stem. When there are large differences among rice accessions, such as contrasting levels of bending stress resistance, it is necessary to comprehensively examine the lodging resistance of each rice accession at different heights. In addition, based on the culm wall area in different transverse sections, the 3D distribution of bending stress can be visualized, and 3D traits such as culm angle, total\_volume\_culm, and

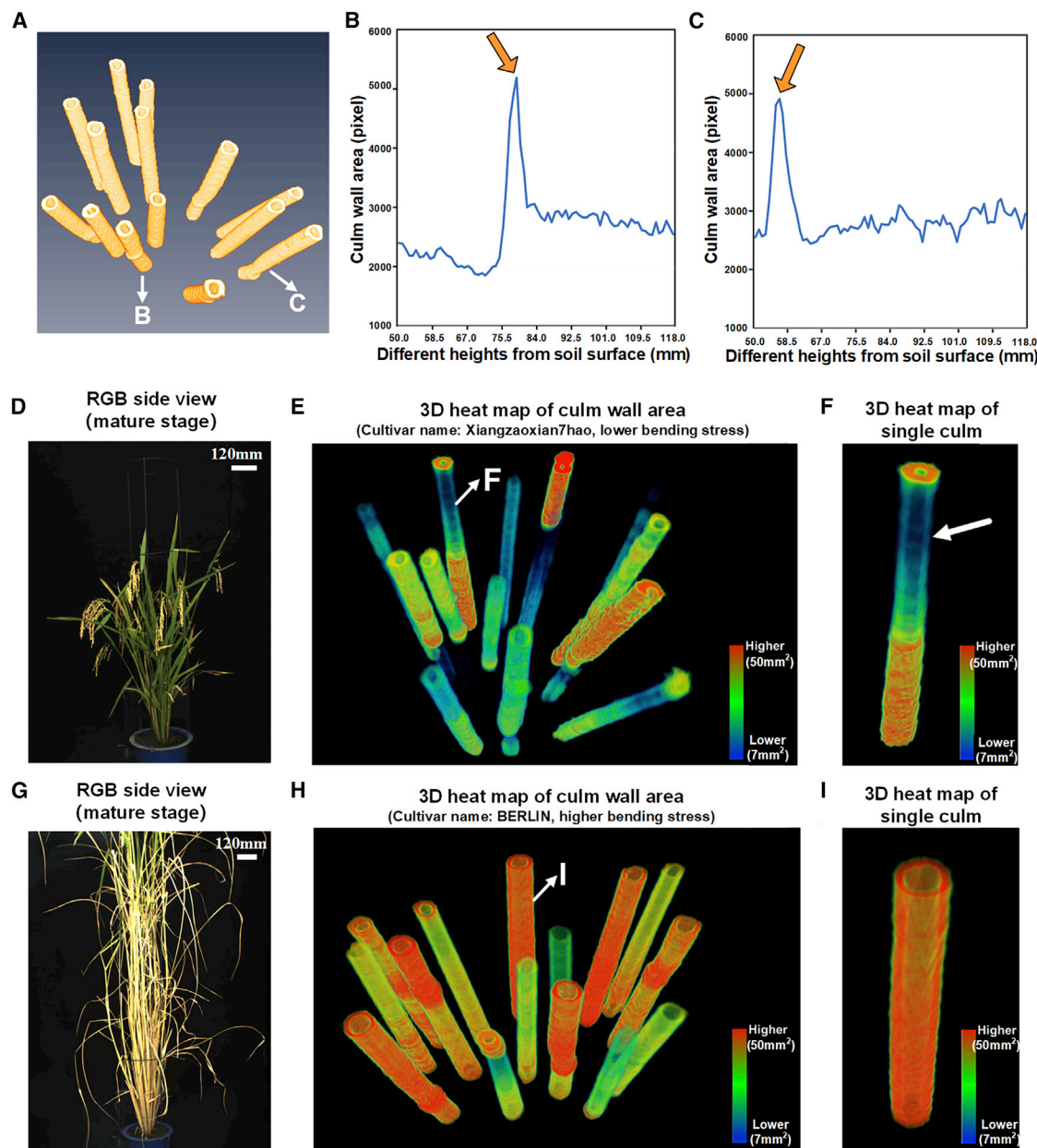


**Figure 7. Evaluation of the calculated culm wall area at different heights and 3D heatmap of culm wall area distribution.**

(A) 3D reconstructed image and (B and C) the distribution of culm wall area at different heights for different tillers, where the red arrows show the node position of each rice culm. RGB side view image (D), 3D heatmap of the wall areas of all culms (E), and 3D heatmap of a single culm (F) from accession Xiangzaoxian7hao, which has lower resistance to bending stress. RGB side view image (G), 3D heatmap of the wall area of all culms (H), and 3D heatmap of a single culm (I) from accession BERLIN, which has higher resistance to bending stress.

total\_SA\_culm can be extracted. In the future, more 3D measurements could be extracted to comprehensively identify rice accessions with higher bending stress resistance. In conclusion, based on a high-throughput micro-CT imaging system and deep learning, we developed a micro-CT image analysis pipeline that rapidly (~4.6 min per plant, including an acquisition time of 2.5 min) and accurately quantified 24 phenotypic traits of rice culms. It also enabled us to visualize the 3D bending stress distribution of rice culms, which will be useful for future high-throughput screening of large rice populations for lodging resistance.

## METHODS

### Plant materials and experimental design

One hundred and four *indica* rice accessions (two samples per accession) with higher or lower bending stress resistance were analyzed in this study (see detailed information on the accessions in [Supplemental Data 1](#) and [Supplemental Table 2](#)). All rice plants were cultivated in plastic pots (235 mm in diameter and 190 mm in height) that contained experimental soil. Each pot was filled with 5 kg of soil (pH 5.45; total nitrogen, 0.241 g/kg; total potassium, 7.20 g/kg; total phosphorus, 0.74 g/kg; alkali-hydrolyzable nitrogen, 144.06 mg/kg; available potassium, 188.64 mg/kg; available phosphorus, 16.81 mg/kg; and organic matter,

## Plant Communications

46.55 g/kg). The experimental conditions are shown in [Supplemental Figure 5](#).

To estimate measurement accuracy, 104 plants at the mature stage (approximately 120 days after sowing) were digitally measured by micro-CT and manually measured to obtain the `major_axis_culm`, `minor_axis_culm`, and `wall_thickness_culm` of the three thickest culms using a Vernier caliper and prostrate tester (DIK-7401, Daiki Rika Kogyo Co., JPN). The average values of the three rice culms were used as the manual measurements of `major_axis_culm`, `minor_axis_culm`, and `wall_thickness_culm`. The measurement position was 40–60 mm from the soil surface.

In our previous work, we quantified three drought-related traits (stay-green, leaf-rolling, and LWC) of 507 rice accessions ([Guo et al., 2018](#)). To analyze the relationship between bending stress and drought resistance, we reanalyzed and compared the same three drought-related traits of the same 104 rice accessions in this study.

In our previous study, 75 traits (CT traits and RGB traits; the traits of rice accessions were calculated independently) were obtained for 234 rice accessions at the tillering stage ([Wu et al., 2019](#)). In this work, the phenotypic traits of 104 rice plants at the tillering stage (approximately 60 days after sowing) were reanalyzed and compared to predict bending stress at the mature stage.

To compare the accuracy of CT and RGB in measuring rice culm diameter, we also manually measured rice culm diameters from the RGB images using the following steps: (1) one of the RGB side view images was selected in NI Vision Assistant software (National Instruments, USA); (2) “Processing Functions: Image,” “Measure,” and “Length” were selected; (3) the three thickest rice culms were observed (consistent with the manual and CT measurements), and three lines were drawn on the culms to represent rice culm diameter; and (4) the three values were averaged to give a final value for rice culm diameter (RGB-manual, [Figure 5C](#)).

### Micro-CT system

The high-throughput micro-CT-RGB imaging system was developed in our previous work ([Wu et al., 2019](#)) and can nondestructively obtain 75 rice phenotypic traits with high efficiency (~4.6 min per plant, including an acquisition time of 2.5 min) during the tillering stage. In this study, a micro-CT image analysis pipeline and deep learning network (SegNet) were used, and the bimodal imaging system was used to nondestructively obtain 24 culm traits at the mature stage to reflect lodging resistance. When using the micro-CT-RGB imaging system to screen rice culms, we can also obtain RGB side view images at the same time ([Wu et al., 2019](#)). From the RGB images, we can evaluate the diameters of rice culms manually using NI Vision Assistant (National Instruments) (see details in the Plant materials and experimental design section). The micro-CT system is composed of nine main elements: an X-ray source (Nova 600, Oxford Instruments, UK), an X-ray source chiller (Nova 600, Oxford Instruments), an X-ray flat panel detector (PaxScan 2520DX, Varian Medical Systems, USA), an RGB camera (AVT Stingray F-504B, Allied Vision Technologies, Germany), a lead chamber, a computer (M6600N, Lenovo, China), a programmable logic controller (CP1H, Omron, Japan), a white light, and a rotation platform (MSMD022G1U, Panasonic, Japan). The main specifications of the micro-CT system inspection unit are shown in [Supplemental Table 2](#).

### Image analysis pipeline using SegNet and LabVIEW

After we obtained the reconstructed rice culm images, each slice needed to be segmented to calculate the culm traits. Image segmentation was performed using a fully convolutional neural network, SegNet ([Vijay et al., 2017](#)). The SegNet architecture is composed of an encoder network to perform convolution and a corresponding decoder network to perform upsampling for pixel-wise classification. The trait extraction was performed in LabVIEW 8.6 (National Instruments), using the following steps.

## Micro-CT for rice lodging phenotyping

(1) We randomly selected 160 original images (slices) as the training set, 20 slices as the validation set, and 20 slices as the test set. To enlarge the training set, we rotated each slice in the training set and adjusted its contrast to generate seven new training samples. The seven new samples included: (1–3) the original slice rotated by 90°, 180°, and 270°; (4) the original slice with the gray value of each pixel multiplied by 0.75 and 32 added; (5) the original slice rotated by 90° with the gray value of each pixel multiplied by 0.75 and 32 added; (6) the original slice rotated by 180° with the gray value of each pixel multiplied by 0.6 and 51 added; and (7) the original slice rotated by 270° with the gray value of each pixel multiplied by 0.6 and 51 added. After data augmentation, the training set included 1280 slices ([Supplemental Note 1](#)).

(2) Because the size of each slice was 1803 × 1803 pixels, which did not meet the input requirements of SegNet, all the slices were expanded to 1920 × 2160 pixels. The gray value of the extended portion of the pixels at the right and bottom edges was set to zero ([Figure 1C](#) and [1E](#)). The enlarged image was then divided into 24 patches, each of which was 360 × 480 pixels. After removing large numbers of patches that contained only background pixels in order to balance the positive and negative pixels in the training set, the final training set contained 10 173 patches, the validation set 480 patches, and the test set 480 patches.

(3) SegNet was trained as shown in the tutorial <http://mi.eng.cam.ac.uk/projects/segnet/tutorial.html> ([Vijay et al., 2017](#)). After 25 440 iterations, the IoU, precision, recall, and F-measure (%) of the 20 original slices in the test set were 0.727%, 0.749%, 0.961%, and 84.2%, respectively. The detailed procedure for training SegNet is described in [Supplemental Note 1](#).

(4) The total number of rice samples in this study was 104, and the number of reconstructed slices for each rice sample was 80; thus, the total slice number was 8320. After the trained SegNet (Culms-SegNet) model was obtained, each of the 8320 reconstructed slices ([Figure 1I](#)) was first expanded to 1920 × 2160 pixels and divided into 24 patches ([Figure 1J](#)). Then, 24 patches of each slice were segmented using the trained SegNet ([Figure 1K](#)) and merged into one slice ([Figure 1L](#)).

(5) After the segmented slice ([Figure 1L](#)) was obtained, the small regions were removed, and erode operations were used to remove noise points (such as the leaf sheath) surrounding the segmented culms ([Figure 1M](#)). After 80 slices were segmented, 3D data points of rice culms were generated, and 24 3D culm traits were calculated. All the culm traits are listed in [Table 1](#), and the main source code is provided in [Supplemental Video 1](#), [Supplemental Note 2](#), our Crop Phenomics Group website ([http://plantphenomics.hzau.edu.cn/download\\_checkiflogin\\_en.action](http://plantphenomics.hzau.edu.cn/download_checkiflogin_en.action)), and a GitHub website (<https://github.com/diwu861125/diwu123456>).

### Three different classification methods

In the present study, SDA training was performed using SPSS v.19 software (IBM, USA) ([Shi et al., 2006](#)), which is a proven technique for classifying rice accessions into higher and lower bending stress resistance groups. SVMs ([Iosifidis and Gabbouj, 2016](#)) are binary classifiers that learn a hyperplane that separates two classes with maximum margins; they are widely used in many classification applications. The libsvm MATLAB toolkit was used to run the SVM model. RF ([Pardo and Sberveglieri, 2008](#)) is a powerful statistical classifier, and the RF classifier is a combination of multiple decision trees. In this paper, SVM and RF were implemented using MATLAB 8.3 software (MathWorks, USA), and the core source code is provided in [Supplemental Notes 3](#) and [4](#).

### DATA AND CODE AVAILABILITY

All phenotypic data can be downloaded in [Supplemental Data 1](#). The source code and user guidelines are available at [http://plantphenomics.hzau.edu.cn/download\\_checkiflogin\\_en.action](http://plantphenomics.hzau.edu.cn/download_checkiflogin_en.action) and <https://github.com/diwu861125/diwu123456>.

## Micro-CT for rice lodging phenotyping

## Plant Communications

### SUPPLEMENTAL INFORMATION

Supplemental Information is available at *Plant Communications Online*.

### FUNDING

This work was supported by grants from the National Key Research and Development Program (2020YFD1000904-1-3), the National Natural Science Foundation of China (31770397), the Fundamental Research Funds for the Central Universities (2662020ZKPY017), and UK grants supported by the Biotechnology and Biological Sciences Research Council (BB/J004464/1, BB/CAP1730/1, BB/CSP1730/1, and BB/R02118X/1).

### AUTHOR CONTRIBUTIONS

D.W. (Di Wu) designed the research, performed the experiments, analyzed the data, and wrote the manuscript. D.W. (Dan Wu) constructed the CNNs. L.D. assisted in constructing the CNNs. H.F., G.D., X.L., K.W., and P.Y. performed the experiments. G.C. performed rice cultivation and rice management. L.X. provided the rice accessions. A.P.G. and J.H.D. assisted in writing the manuscript and improving the work. W.Y. supervised the project, designed the research, and wrote the manuscript.

### DECLARATION OF INTERESTS

The authors declare that they have no competing interests.

Received: June 27, 2020

Revised: November 7, 2020

Accepted: January 26, 2021

Published: ■ ■ ■ ■ ■, ■ ■ ■

### REFERENCES

- Beddington, J.** (2010). Food security: contributions from science to a new and greener revolution. *Phil T R. Soc. B* **365**:61–71.
- Berry, P.M., Sylvester-Bradley, R., and Berry, S.** (2007). Ideotype design for lodging resistant wheat. *Euphytica* **154**:165–179.
- Brown, M.E., and Funk, C.C.** (2008). Food security under climate change. *Science* **319**:580–581.
- Chu, T., Starek, M.J., Brewer, M.J., Murray, S.C., and Pruter, L.S.** (2017). Assessing lodging severity over an experimental maize (*Zea mays* L.) field using UAS images. *Remote Sens.* **9**:923–946.
- Daly, K.R., Mooney, S.J., Bennett, M.J., Crout, N.M., Roose, T., and Tracy, S.R.** (2015). Assessing the influence of the rhizosphere on soil hydraulic properties using X-ray computed tomography and numerical modelling. *J. Exp. Bot.* **66**:2305–2314.
- Du, J., Zhang, Y., Guo, X., Ma, L., Pan, X., and Zhao, C.** (2016). Micron-scale phenotyping quantification and three-dimensional microstructure reconstruction of vascular bundles within maize stalks based on micro-CT scanning. *Funct. Plant Biol.* **44**:10–22.
- Duan, C., Wang, B., Wang, P., Wang, P., Wang, D., and Cai, S.** (2004). Relationship between the minute structure and the lodging resistance of rice stems. *Colloid Surf. B* **35**:155–158.
- Flavel, R.J., Guppy, C.N., Tighe, M., Watt, M., McNeill, A., and Young, L.M.** (2012). Non-destructive quantification of cereal roots in soil using high-resolution X-ray tomography. *J. Exp. Bot.* **63**:2503–2511.
- Fung, G.M., and Mangasarian, O.L.** (2005). Mangasarian, multicategory proximal support vector machine classifiers. *Mach. Learn.* **59**:77–97.
- Furbank, R.T., and Tester, M.** (2011). Phenomics—technologies to relieve the phenotyping bottleneck. *Trends Plant Sci.* **16**:635–644.
- Granitto, P.M., Furlanello, C., Biasioli, F., and Gasperi, F.** (2006). Recursive feature elimination with random forest for PTR-MS analysis of agroindustrial products. *Chemometr. Intell. Lab.* **83**:83–90.
- Guo, Z., Yang, W., Chang, Y., Ma, X., Tu, H., Xiong, F., Jiang, N., Feng, H., Huang, C., Yang, P., et al.** (2018). Genome-wide association studies of image traits reveal genetic architecture of drought resistance in rice. *Mol. Plant* **11**:789–805.
- Hedden, P.** (2013). The genes of the green revolution. *Trends Genet.* **19**:5–9.
- Houle, D., Govindaraju, D.R., and Omholt, S.** (2010). Phenomics: the next challenge. *Nat. Rev. Genet.* **11**:855–866.
- Hughes, N., Askew, K., Scotson, C.P., Williams, K., Sauze, C., Corke, F., Doonan, J.H., and Nibau, C.** (2017). Non-destructive, high-content analysis of wheat grain traits using X-ray micro computed tomography. *Plant Methods* **13**:76–85.
- Iosifidis, A., and Gabbouj, M.** (2016). Multi-class support vector machine classifiers using intrinsic and penalty graphs. *Pattern Recogn* **55**:231–246.
- Jin, S., Su, Y., Gao, S., et al.** (2018). Deep learning: individual maize segmentation from terrestrial Lidar data using faster R-CNN and regional growth algorithms. *Front. Plant Sci.* **9**:866.
- Kamilaris, A., and Francesc, X.** (2018). Deep learning in agriculture: a survey. *Comput. Electron. Agric.* **147**:70–90.
- Kashiwagi, T., and Ishimaru, K.** (2004). Identification and functional analysis of a locus for improvement of lodging resistance in rice. *Plant Physiol.* **134**:676–683.
- Li, X., Qian, Q., Fu, Z., Wang, Y., Xiong, G., Zeng, D., Wang, X., Liu, X., Teng, S., Hiroshi, F., et al.** (2003). Control of tillering in rice. *Nature* **422**:618–621.
- Li, Z., Chen, Z., Wang, L., Liu, J., and Zhou, Q.** (2014). Area extraction of maize lodging based on remote sensing by small unmanned aerial vehicle. *Trans. Chin Soc. Agric. Eng.* **30**:207–213.
- Liu, T., Li, R., Zhong, X., Jiang, M., Jin, X., Zhou, P., Liu, S., Sun, C., and Guo, W.** (2018). Estimates of rice lodging using indices derived from UAV visible and thermal infrared images. *Agr For. Meteorol.* **252**:144–154.
- Liu, Y., Cen, C., Che, Y., Ke, R., Ma, Y., and Ma, Y.** (2020). Detection of maize tassels from UAV RGB imagery with faster R-CNN. *Remote Sens* **12**:1–13.
- Lontoc-Roy, M., Dutilleul, P., Prasher, S.O., Han, L., Brouillet, T., and Smith, D.L.** (2006). Advances in the acquisition and analysis of CT scan data to isolate a crop root system from the soil medium and quantify root system complexity in 3-D space. *Geoderma* **137**:231–241.
- Mallios, R.R.** (2001). Predicting class II MHC/peptide multi-level binding with an iterative stepwise discriminant analysis meta-algorithm. *Bioinformatics* **17**:942–948.
- Pardo, M., and Sberveglieri, G.** (2008). Random forests and nearest shrunken centroids for the classification of sensor array data. *Sens. Actuat. B Chem.* **131**:93–99.
- Rahmoonfar, M., and Sheppard, C.** (2017). Deep count: fruit counting based on deep simulated learning. *Sensors* **17**:905–914.
- Ren, S., He, K., Girshick, R., and Sun, J.** (2017). Faster R-CNN: towards real-time object detection with region proposal networks. *IEEE Trans. Pattern Anal. Mach. Intellig.* **39**:1137–1149.
- Ryu, J., Hwang, B.G., Kim, Y.X., and Lee, S.** (2016). Direct observation of local xylem embolisms induced by soil drying in intact *Zea mays* leaves. *J. Exp. Bot.* **67**:2617–2626.
- Shi, Z., Cheng, J., Huang, M., and Zhou, L.** (2006). Assessing reclamation levels of coastal saline lands with integrated stepwise discriminant analysis and laboratory hyperspectral data. *Pedosphere* **16**:154–160.
- Strange, H., Zwiggelaar, R., Sturrock, C., and Mooney, S.** (2015). Automatic estimation of wheat grain morphometry from CT data. *Funct. Plant Biol.* **42**:452–459.
- Tracy, S.R., Black, C.R., Robert, J.A., McNeill, A., Davidson, R., and Tester, M.** (2012). Quantifying the effect of soil compaction on three varieties of wheat (*Triticum aestivum*, L.) using X-ray micro computed tomography (CT). *Plant Soil* **353**:195–208.



## Plant Communications

- Tracy, S.R., Black, C.R., Roberts, J.A., Dodd, L.C., and Mooney, S.** (2015). Using X-ray computed tomography to explore the role of abscisic acid in moderating the impact of soil compaction on root system architecture. *Environ. Exp. Bot.* **110**:11–18.
- Tracy, S.R., Gómez, J.F., Sturrock, C.J., Wilson, Z.A., and Ferguson, A.C.** (2017). Non-destructive determination of floral staging in cereals using X-ray micro computed tomography ( $\mu$ CT). *Plant Methods* **13**:9–17.
- Uzal, L.C., Grinblat, G.L., Namías, R., Larese, M.G., Bianchi, J.S., Morandi, E.N., and Granitto, P.M.** (2018). Seed-per-pod estimation for plant breeding using deep learning. *Comput. Electron. Agric.* **150**:196–204.
- Vijay, B., Alex, K., and Roberto, C.** (2017). SegNet: a deep convolutional encoder-decoder architecture for image segmentation. *IEEE Trans. Pattern Anal. Mach. Intellig.* **39**:2481–2495.
- Wang, L., Xu, Y., Zhang, C., Ma, Q., Joo, S.H., Kim, S.K., Xu, Z., and Chong, K.** (2008). OsLIC, a novel CCCH-type zinc finger protein with transcription activation, mediates rice architecture via brassinosteroids signaling. *PLoS One* **10**:3521–3532.

## Micro-CT for rice lodging phenotyping

- Wang Q, Qi F.** (2019). Tomato Diseases Recognition Based on Faster RCNN. 2019 10th International Conference on Information Technology in Medicine and Education (ITME). pp:772–776.
- Wang, Y., and Li, J.** (2005). The plant architecture of rice (*Oryza sativa*). *Plant Mol. Biol.* **59**:75–84.
- Wu, D., Guo, Z., Ye, J., Feng, H., Liu, J., Chen, G., Zheng, J., Yan, D., Yang, X., Xiong, X., et al.** (2019). Combining high-throughput micro-CT-RGB phenotyping and genome-wide association study to dissect the genetic architecture of tiller growth in rice. *J. Exp. Bot.* **70**:545–561.
- Yang, M.D., Huang, K.S., Kuo, Y.H., Tasi, H.P., and Lin, L.M.** (2017). Spatial and spectral hybrid image classification for rice lodging assessment through UAV imagery. *Remote Sens* **9**:583–601.
- Zhang, Y., Du, J., Wang, J., Ma, L., Lu, X., Pan, X., Guo, X., and Zhan, C.** (2018). High-throughput micro-phenotyping measurements applied to assess stalk lodging in maize (*Zea mays* L.). *Biol. Res.* **51**:40–53.
- Zhang, Q.** (2007). Strategies for developing green super rice. *Proc. Natl. Acad. Sci. U S A* **104**:16402–16409.